Eur. Phys. J. A (2012) **48**: 74
DOI 10.1140/epja/i2012-12074-9

THE EUROPEAN PHYSICAL JOURNAL A

Regular Article – Experimental Physics

Study of exclusive one-pion and one-eta production using hadron and dielectron channels in pp reactions at kinetic beam energies of 1.25 GeV and 2.2 GeV with HADES

HADES Collaboration

G. Agakishiev[5], H. Alvarez-Pol[15], A. Balanda[2], R. Bassini[10], M. Böhmer[8], H. Bokemeyer[3], J.L. Boyard[13], P. Cabanelas[15], S. Chernenko[5], T. Christ[8], M. Destefanis[9], F. Dohrmann[4], A. Dybczak[2], T. Eberl[8], L. Fabbietti[7], O. Fateev[5], P. Finocchiaro[1], J. Friese[8], I. Fröhlich[6], T. Galatyuk[6,B], J.A. Garzón[15], R. Gernhäuser[8], C. Gilardi[9], M. Golubeva[11], D. González-Díaz[C], F. Guber[11], M. Gumberidze[13], T. Hennino[13], R. Holzmann[3], A. Ierusalimov[5], I. Iori[10,E], A. Ivashkin[11], M. Jurkovic[8], B. Kämpfer[4,D], K. Kanaki[4], T. Karavicheva[11], I. Koenig[3], W. Koenig[3], B.W. Kolb[3], R. Kotte[4], A. Kozuch[2,F], F. Krizek[14], W. Kühn[9], A. Kugler[14], A. Kurepin[11], S. Lang[3], K. Lapidus[7], T. Liu[13], L. Maier[8], J. Markert[6], V. Metag[9], B. Michalska[2], E. Morinière[13], J. Mousa[12], M. Münch[3], C. Müntz[6], L. Naumann[4], J. Otwinowski[2], Y.C. Pachmayer[6], V. Pechenov[3], O. Pechenova[6], T. Pérez Cavalcanti[9], J. Pietraszko[6], V. Pospísil[14], W. Przygoda[2], B. Ramstein[13], A. Reshetin[11], M. Roy-Stephan[13], A. Rustamov[3], A. Sadovsky[11], B. Sailer[8], P. Salabura[2], M. Sánchez[15], A. Schmah[A], E. Schwab[3], Yu.G. Sobolev[14], S. Spataro[1,9,G], B. Spruck[9], H. Ströbele[6], J. Stroth[3,6], C. Sturm[3], A. Tarantola[6], K. Teilab[6], P. Tlusty[14], A. Toia[9], M. Traxler[3], R. Trebacz[2], H. Tsertos[12], V. Wagner[14], M. Wisniowski[2], T. Wojcik[2], J. Wüstenfeld[4], S. Yurevich[3], Y. Zanevsky[5], and P. Zumbruch[3,a]

[1] Istituto Nazionale di Fisica Nucleare - Laboratori Nazionali del Sud, 95125 Catania, Italy
[2] Smoluchowski Institute of Physics, Jagiellonian University of Cracow, 30-059 Kraków, Poland
[3] GSI Helmholtz-Zentrum für Schwerionenforschung GmbH, 64291 Darmstadt, Germany
[4] Institut für Strahlenphysik, Helmholtz-Zentrum Dresden-Rossendorf, 01314 Dresden, Germany
[5] Joint Institute of Nuclear Research, 141980 Dubna, Russia
[6] Institut für Kernphysik, Goethe-Universität, 60438 Frankfurt, Germany
[7] Excellence Cluster "Origin and Structure of the Universe", 85748 Garching, Germany
[8] Physik Department E12, Technische Universität München, 85748 Garching, Germany
[9] II.Physikalisches Institut, Justus Liebig Universität Giessen, 35392 Giessen, Germany
[10] Istituto Nazionale di Fisica Nucleare, Sezione di Milano, 20133 Milano, Italy
[11] Institute for Nuclear Research, Russian Academy of Science, 117312 Moscow, Russia
[12] Department of Physics, University of Cyprus, 1678 Nicosia, Cyprus
[13] Institut de Physique Nucléaire (UMR 8608), CNRS/IN2P3 - Université Paris Sud, F-91406 Orsay Cedex, France
[14] Nuclear Physics Institute, Academy of Sciences of Czech Republic, 25068 Rez, Czech Republic
[15] Departamento de Física de Partículas, Univ. de Santiago de Compostela, 15706 Santiago de Compostela, Spain

[A] *Also at*: Lawrence Berkeley National Laboratory, Berkeley, USA.
[B] *Also at*: ExtreMe Matter Institute EMMI, 64291 Darmstadt, Germany.
[C] *Also at*: Technische Universität Darmstadt, 64289 Darmstadt, Germany.
[D] *Also at*: Technische Universität Dresden, 01062 Dresden, Germany.
[E] *Also at*: Dipartimento di Fisica, Università di Milano, 20133 Milano, Italy.
[F] *Also at*: Panstwowa Wyzsza Szkola Zawodowa, 33-300 Nowy Sacz, Poland.
[G] *Also at*: Dipartimento di Fisica Generale and INFN, Università di Torino, 10125 Torino, Italy.

Received: 6 March 2012 / Revised: 10 April 2012
Published online: 29 May 2012

Communicated by M. Guidal

Abstract. We present measurements of exclusive $\pi^{+,0}$ and η production in pp reactions at 1.25 GeV and 2.2 GeV beam kinetic energy in hadron and dielectron channels. In the case of π^+ and π^0, high-statistics invariant-mass and angular distributions are obtained within the HADES acceptance as well as acceptance-corrected distributions, which are compared to a resonance model. The sensitivity of the data to the yield

and production angular distribution of $\Delta(1232)$ and higher-lying baryon resonances is shown, and an improved parameterization is proposed. The extracted cross-sections are of special interest in the case of $pp \to pp\eta$, since controversial data exist at 2.0 GeV; we find $\sigma = 0.142 \pm 0.022$ mb. Using the dielectron channels, the π^0 and η Dalitz decay signals are reconstructed with yields fully consistent with the hadronic channels. The electron invariant masses and acceptance-corrected helicity angle distributions are found in good agreement with model predictions.

1 Introduction

Meson production in nucleon-nucleon reactions in the kinetic beam energy range 1–2 GeV tests an important sector of strong interaction on the hadron level. It is the subject of extensive studies by both experiment and theory with the aim to establish eventually the link of hadron physics to QCD as fundamental theory. Most of the available high-statistics data originate from recent near-threshold measurements, at excess energies < 150 MeV, performed at the SATURNE, CELSIUS and COSY facilities. Phenomenological models, usually adjusted to data of these reactions, serve as step towards a concise theoretical description. Such models are based on, for instance, the one-boson exchange (OBE) approximation describing the production amplitudes by a coherent sum of meson, nucleon and baryon-resonance currents. They reveal that meson production is a complex process with important contributions from nucleon-nucleon final-state interactions and interferences between the contributing reaction channels even within a tree-level approach. This situation often leads to ambiguous model descriptions of the experimental results (for a review, see [1]). For higher energies, *i.e.* excess energies > 150 MeV, the data base is more scarce and originates mainly from low-statistics bubble-chamber experiments [2].

The production of π and η mesons in nucleon-nucleon collisions is of particular importance because of their coupling to baryonic resonances. Hence, experimental data on one-π and one-η production provide quantitative information on hadronic interactions, as well as resonance excitations and resonance properties.

Cross sections for pion production in the beam energy range from 0.6 to 1.5 GeV (excess energies between 140 and 500 MeV) have been provided in the past by many experiments [3–8]. Meanwhile, also the precision of the measurements of differential distributions, which is essential for unravelling the reaction mechanism, has been improved [9–15]. The dominance of the intermediate $\Delta(1232)$ production and the peripheral character of the reaction, which increases with energy, stand out very clearly in this region. Comparison of the shape of various differential distributions from both exclusive reactions $pp \to pp\pi^0$ and $pp \to pn\pi^+$ in the range 0.6–0.94 GeV to calculations within the one-pion exchange (OPE) show a nice agreement [10,11]. However, the magnitude of the cross-sections for both reactions, regardless of the choice of the form of π-nucleon interaction, is explained by the models within an accuracy of 20–30% only. This points to some missing elements in the assumed reaction mechanism, as for example the exchange of heavier mesons, contributions of heavier resonances or/and non-resonant π production, as demonstrated by a recent detailed analysis of $pp \to pn\pi^+$ and $pp \to pp\pi^0$ reactions at a beam energy of 0.94 GeV within the framework of a partial-wave analysis [15].

At beam energies higher than 1.5 GeV, the interpretation of the low-statistics bubble-chamber data [16–18] was based on the isobar model assuming an incoherent sum of contributions from the decays of various baryon resonances into pions. However, large uncertainties remain, due to the limited statistical significance of the corresponding experimental results. Further progress in the understanding of meson production in $p + p$ interactions thus requires new high-statistics data.

For the one-η production, precise data have been collected close to the reaction threshold (excess energies below 120 MeV) [19–28] and compared to various OBE models (for a survey, cf. [1]). Most of the calculations indicate a dominant role of resonances, in particular the $N^*(1535)$ formed via the exchange of virtual pseudoscalar (π, η) and vector (ρ, ω) mesons. However, the models differ in the description of how the resonance is excited, which is due to the uncertainty in the nucleon-meson-N^* couplings. Better constraints can be obtained from differential distributions and polarization observables, as demonstrated in [29]. The dominance of $N^*(1535)$ seems also to persist at higher beam energies (2–3 GeV), as shown by a detailed analysis of the $pp\eta$ Dalitz distributions by the DISTO Collaboration [30]. The latter work, however, does not provide absolute cross-sections which are very important for the quantitative evaluation of the role of resonances.

Under the assumption that intermediate baryon resonances play a dominant role in π, η and ρ production, a model was developed [31] based on an incoherent sum of various resonance contributions. The matrix element of the $\Delta(1232)$ production was calculated within the OPE model [32], which had been adjusted to available differential distributions of pion production in the $pp \to pn\pi^+$ channel at incident kinetic energies in the range 0.9–1.5 GeV. The other matrix elements were kept constant and were determined by fitting the total meson production cross-sections.

[a] e-mail: ramstein@ipno.in2p3.fr (corresponding author)

Meson production is an important ingredient of microscopic transport models which were developed to describe heavy-ion collisions. Such approaches rely on a realistic treatment of elementary nucleon-nucleon and meson-nucleon interactions, as described in the previous paragraphs, to calculate double-differential cross-sections of the produced particles [33–38].

Electromagnetic decays of mesons and baryon resonances are sources of e^+e^- (dielectron) pairs which play a prominent role in heavy-ion physics as penetrating probes of nuclear and hadronic media. Therefore, data on π, η, and baryon resonance production in proton-proton interactions are essential for the understanding of e^+e^- pair production in p + p, p + nucleus and nucleus-nucleus collisions. Recent precise measurements of the HADES Collaboration underline the need to understand elementary sources of e^+e^- pairs for the interpretation of heavy-ion data [39–42]. It turns out that the baryon resonances are especially important. They contribute to the dielectron spectra via direct Dalitz decay, $\Delta \to Ne^+e^-$, and via two-step processes in which the resonance decays into a nucleon and a meson with a subsequent e^+e^- pair produced in the Dalitz decay of the meson (*e.g.*, $\Delta(1232) \to N\pi^0$ followed by $\pi^0 \to \gamma e^+e^-$ or $N(1535) \to N\eta$ followed by $\eta \to \gamma e^+e^-$) or two-body decays of the produced mesons (*e.g.*, $N(1520) \to N\rho$ followed by $\rho \to e^+e^-$).

At higher beam energies [43], the dielectron yield is a complicated cocktail resulting from decays of many mesons and baryon resonances, but the main dielectron sources in nucleon-nucleon collisions are still the π^0 Dalitz decays for dielectron invariant masses $M_{ee} < 0.135\,\mathrm{GeV}/c^2$, the η Dalitz decay contribution for $0.14\,\mathrm{GeV}/c^2 < M_{ee} < 0.547\,\mathrm{GeV}/c^2$ and Dalitz decays of baryon resonances and light vector mesons (ρ and ω) for $M_{ee} > 0.6\,\mathrm{GeV}/c^2$.

In the past, experiments studying p + p and π+p interactions have either analyzed the hadronic or leptonic final states. The HADES apparatus [44] allows for the first time to measure hadron and e^+e^- pair final states simultaneously with high statistics. With such data, it is possible to achieve a consistent description of meson production in p + p reactions in the hadron as well as in the dielectron channel. In this article, we present the first step in this direction and compare experimental results from the analysis of three reaction channels $pp \to pn\pi^+$, $pp \to pp\pi^0$, and $pp \to pp\eta$ measured at kinetic beam energies of 2.2 GeV and of the corresponding dielectron channels $pp \to pp\pi^0 \to ppe^+e^-\gamma$ and $pp \to pp\eta \to ppe^+e^-\gamma$ obtained at a kinetic beam energy of 2.2 GeV. At 1.25 GeV, which is below the threshold of η production in pp reactions, only the reactions involving pions were analyzed. As reference model, we use predictions of the aforementioned resonance model of [31], complemented with experimental results [30]. Differential spectra have been measured with high statistics providing strong constraints on the production mechanisms as well as on the different resonance contributions.

The polarization of virtual photons has never been measured in the Dalitz decays of the pseudoscalar mesons, although the distributions of the respective angles of the emitted lepton with respect to the virtual photon direction (the so-called helicity) have been predicted for several sources [45]. It has also been suggested that such distributions can be used as important "fingerprints" to distinguish between different dielectron sources in the inclusive measurements. Indeed, as shown in [46], virtual photon polarization appears to be a very important characteristics of the dielectron excess radiation originating from the hot and dense hadronic matter created in heavy-ion collisions at SPS energies. In contrast to the situation at the SPS, similar measurements at SIS18 energies show a sizable anisotropy in the helicity distributions [42]. Therefore, it is desirable to determine the relevant distributions for the π^0 and η mesons, as well as for baryon resonances, such as the $\Delta(1232)$, and bremsstrahlung in p + p collisions. In this work, we present such a measurement for the η Dalitz decay which has been isolated in the $pp \to ppe^+e^-\gamma$ reaction channel.

Our paper has the following structure. The experimental set-up and event reconstruction will be briefly described in sect. 2. The data analysis methods and simulation tools are presented in sects. 3 and 4. Section 5 is devoted to the discussion of the results. We draw conclusions in sect. 6.

2 Experimental aspects

2.1 Detector overview

The High Acceptance Di-Electron Spectrometer (HADES) consists of six identical sectors covering polar angles between 18° and 85° and between 65 and 90% of the azimuthal range. While a detailed description of the set-up can be found in [44], we summarize here only the features relevant for the present analyses. Proton beams with intensities up to 10^7 particles/s were directed to a 5 cm long liquid-hydrogen target of 1% interaction probability. The momenta of the produced particles are deduced from the hits in the four drift chamber planes (two before and two after the magnetic field zone) using a Runge-Kutta algorithm [44]. The momentum resolution is 2–3% for protons and pions and 1–2% for electrons, depending on momentum and angle [44]. The trigger for the HADES experiments consists of two stages: The first-level trigger (LVL1) is built on different configurations of hit multiplicity measurements in two plastic scintillator walls for polar angles larger (TOF) and smaller (TOFINO) than 45°, respectively. The second-level trigger (LVL2) selects $e^\pm$ candidates defined by a Ring Imaging Cherenkov (RICH) detector and information from TOF and an electromagnetic shower detector (Pre-Shower) behind TOFINO. The analysis of hadronic channels was based on LVL1 triggered events selected by either of the two following configurations: The first required a coincidence between two hits in two opposite sectors of the time-of-flight detectors, with at least one in the TOFINO. This configuration was optimized for the selection of pp elastic-scattering events and also used for the $pp \to pp\pi^0$ and $pp \to pn\pi^+$ reactions. The second configuration was based on a

Table 1. Investigated reaction channels for exclusive π and η production reactions.

Reaction	Meson decay channel	Measured exit channel	Incident energy
$pp \to pn\pi^+$	–	$\pi^+p(n)$	1.25, 2.2 GeV
$pp \to pp\pi^0$	all	pp (π^0)	1.25, 2.2 GeV
	$\pi^0 \to \gamma e^+e^-$ (BR 1.12%)	ppe^+e^- (γ)	2.2 GeV
$pp \to pp\eta$	$\eta \to \pi^+\pi^-\pi^0$ (BR 22.7%)	$pp\pi^+\pi^-$ (π^0)	2.2 GeV
	$\eta \to \gamma e^+e^-$ (BR 0.68%)	ppe^+e^- (γ)	2.2 GeV

charged particle multiplicity of four or more, at least one hit in the TOFINO and at least two signals in opposite sectors. This selection was used for the reconstruction of $pp \to pp\eta$ hadronic and dielectron channels ($\eta \to \pi^+\pi^-\pi^0$ and $\eta \to \gamma e^+e^-$) as well as $pp \to pp\pi^0$ dielectron channels ($\pi^0 \to \gamma e^+e^-$) in 2.2 GeV collisions. For the π^0 and η electromagnetic Dalitz decay measurements, in addition to the latter LVL1 configuration, a LVL2 decision was requested, *i.e.* at least one electron candidate in the RICH.

2.2 Event reconstruction

Five different final states were used for the study of exclusive π and η production in pp reactions, as summarized in table 1. An important feature of the HADES apparatus, which is exploited in the present analysis, is the ability to measure both hadrons [47,48] and electrons [39–41] in the same experimental run. Of special importance for the analysis of the dielectron channels is the suppression of tracks produced by photon conversion and consequently the reduction of the combinatorial background [44]. This is achieved using criteria related to the track quality and the distance and opening angle between neighbouring tracks. Finally, only e^+e^- pairs with an opening angle larger than 9° were propagated to the physics analysis. The remaining combinatorial background is subtracted from the measured unlike sign pair yields, using the arithmetical mean of the like sign pair (e^+e^+ and e^-e^-) yield in the same event.

Since the RICH is hadron blind in the given energy range and the particle multiplicity is low, electrons and positrons are selected using only the matching of a charged track reconstructed in the drift chambers and a ring pattern in the RICH detector. Particle identification (PID) for pions and protons is provided by the correlation between the velocity ($\beta = v/c$) obtained from TOF or TOFINO scintillator walls and the momentum deduced from the track deflection in the magnetic field [44]. The start signal for the time measurements was taken from the fastest signal from the scintillator wall. To reconstruct the time of flight for each particle, a dedicated method was developed [44], using the identification of one reference particle, the time of flight of which can be calculated.

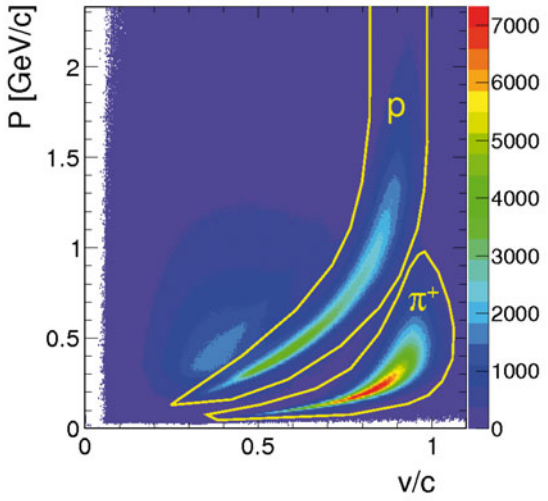

Fig. 1. (Color online) Correlation between momentum (p) and velocity (v/c) for particles without a RICH signal and with curvature corresponding to a positive charge. The overlaid yellow curves indicate graphical cuts to select protons and pions.

When a e^+e^- pair was present in the exit channel, one of the leptons could be used as the reference particle. For events without electron candidates but containing a negatively charged particle, it was used as a reference particle and assigned the pion mass. When only two positive hadrons were observed in the final state, two hypotheses were tested: 1) the presence of two protons (2p events) and 2) the presence of one pion and one proton (π^+p events). For each hypothesis, both hadrons could be used as reference particles, hence providing an additional consistency check. In all the cases described above, the time of flight of the reference particle was calculated, and the velocities of all the other products were then deduced, using only the time-of-flight differences to the reference particle. The correlation between velocity and momentum of all particles was then used to reject the wrong hypotheses and to assign the final PID of all particles. Figure 1 displays such a correlation for positively charged tracks without signal in the RICH. The efficiency of the PID procedure was higher than 90% for both pions and protons. In addition, in the case of the four-particle exit channels, the algorithm was checked in a dedicated experiment with a low beam intensity using a START detector, as discussed in [44].

2.3 Acceptance and efficiency considerations

The spectrometer acceptance, detector efficiency and resolution as well as the analysis cuts necessary to extract the signal introduce important constraints on the determination of the cross-sections and on the comparison of the experimental distributions to model predictions. For the HADES case, to compensate acceptance losses due to spectrometer geometry and extract 4π integrated yields, extrapolation into the unmeasured regions of the phase space is usually achieved by means of a model. The reliability of the model to describe the shape of the relevant

distributions also in the unmeasured regions determines the systematic errors of the acceptance corrections.

On the other hand, direct comparisons of theoretical and experimental distributions can also be made inside the HADES acceptance using dedicated filters. For this purpose, the acceptances and efficiencies for the different particles (*i.e.*, electrons, pions and protons) were separately tabulated in matrices as a function of momentum, azimuthal and polar angles. The matrix coefficients have been determined using full GEANT simulations, with all reaction products processed through the detector, and analysed with the same programmes as done for real events. The resulting acceptance matrices describe the HADES fiducial volume only and can be applied as a filter to events generated by models. The corresponding efficiency matrices account for the detection and reconstruction process and have been used to correct the experimental data event by event. In addition, an emulator of the trigger condition was applied both on experimental data and simulated events. In the case of the two-hit trigger, however, the data were corrected for the condition of having at least one particle in the TOFINO. The detection and reconstruction efficiency was typically 90% for protons and pions and about 50% for electrons. In addition, the yields measured in the e^+e^- channels were corrected for the LVL2 efficiency. The latter was calculated by comparing the $pp \to pp e^+ e^- X$ yield in unbiased LVL1 events to the yield obtained with both LVL1 and LVL2 conditions; in this way a LVL2 efficiency of $90 \pm 5\%$ was obtained.

The momentum resolution parameters were determined from the simulations in bins of momentum and polar and azimuthal angles and rescaled to match the resolution determined experimentally using the elastic pp scattering [44]. The acceptance matrices and resolution parameters, necessary to filter and smear the model generated particle distributions before comparing to HADES efficiency corrected data, are available from the authors upon request.

2.4 Normalization procedure using elastic scattering

The normalization of the experimental yield is obtained using the analysis of events produced in elastic scattering. Momentum conservation in the pp elastic scattering reaction leads to the two following relations between the polar angles θ_1 and θ_2 and azimuthal angles ϕ_1 and ϕ_2 of both protons:

$$|\phi_1 - \phi_2| = 180^\circ, \tag{1}$$

$$\tan\theta_1 \tan\theta_2 = \frac{1}{\gamma_{CM}^2}, \tag{2}$$

where γ_{CM} is the Lorentz factor of the center-of-mass system. The elastic events were selected by an elliptic cut in the $(|\phi_1 - \phi_2|, \tan\theta_1 \tan\theta_2)$ plane, with semi-axes corresponding to approximately 3σ for each variable, *i.e.* $\pm 2.4^\circ$ for $|\phi_1 - \phi_2|$ and $\sigma = 0.027$ for $\tan\theta_1 \tan\theta_2$. The angular distributions of the resulting event ensemble is corrected for efficiency and compared to a simulation which uses the high-precision data from the EDDA experiment [49] as input, as shown in fig. 2 for the 1.25 GeV incident energy case. The histogram in fig. 2 represents the angular distribution of events generated by PLUTO [50,51] according to the parameterization of EDDA data and subjected to the HADES filter, as described in more details in sect. 2.3. The shape of the angular distribution is well reproduced, demonstrating that the angular dependence of the efficiency correction is under control. The cut for angles larger than 62° reflects the cut on the forward partner at about 18°, which is due to the detector acceptance. The experimental yield was scaled in order to reproduce the simulated yield inside the HADES acceptance. The resulting factors are used for the normalization of the differential cross-sections and have a precision of about 6% at 1.25 GeV and 11% at 2.2 GeV, reflecting mainly the uncertainty on the global efficiency of the reconstruction and analysis.

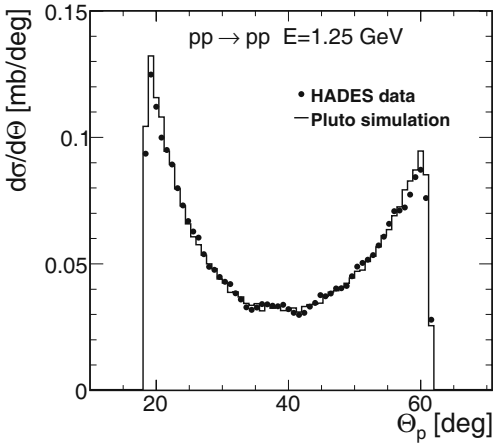

Fig. 2. Angular distribution in the laboratory system of measured pp elastic events (full dots) compared to PLUTO simulations (full histogram) using the angular distributions of [49] as input.

3 Data analysis

3.1 Hadronic channels

3.1.1 Selection of $pp \to pp\pi^0$ and $pp \to pn\pi^+$ channels

To study the $pp \to pp\pi^0$ and $pp \to pn\pi^+$ channels, only the events with two protons (2p) or one proton and one π^+ ($p\pi^+$) have been considered, respectively [52,53]. The selection of both channels is based on the requirement for the missing mass to the system of the two detected charged particles to be close to the missing neutral particle mass. For the events with two detected protons, the distribution of the squared missing mass to the two-proton system ($M^2_{miss}(p,p)$), shown in fig. 3, present for both energies a prominent asymetric peak close to zero. This contribution, clearly due to the elastic scattering, nicely fulfills the corresponding angular correlation (see sect. 2.4), as shown by the dashed histogram. The different widths of these peaks at both energies as well as the better separation of the one-pion contribution at 1.25 GeV result from the resolution on the proton momentum. In addition, these spectra

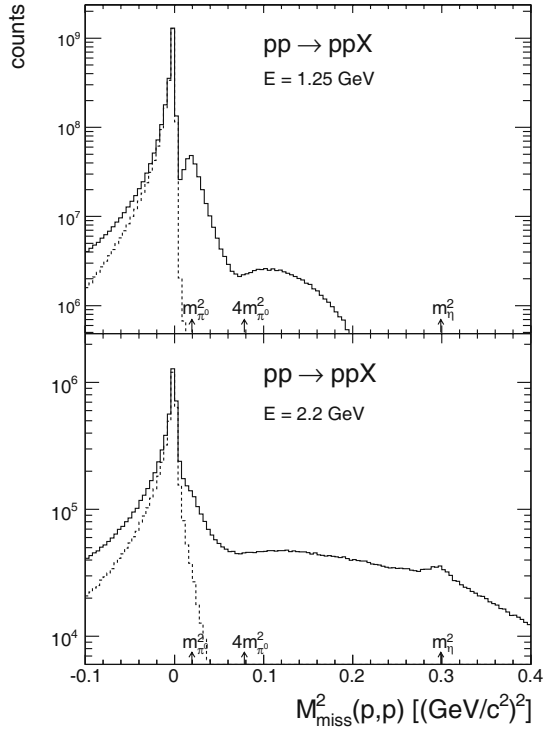

Fig. 3. Squared missing-mass spectra for the reaction pp → pp$X$ at 1.25 GeV (top) and 2.2 GeV (bottom). The dashed histogram shows the events selected by the elastic scattering angular correlations eqs. (1) and (2).

reflect the larger phase space available for inelastic processes at 2.2 GeV. The contribution of the 2π contribution, visible for $M^2_{miss}(\mathrm{p,p})$ larger than $0.08\,(\mathrm{GeV}/c^2)^2$, is clearly enhanced and the η meson production shows up for $M^2_{miss}(\mathrm{p,p})$ around $0.3\,(\mathrm{GeV}/c^2)^2$.

To proceed with the selection of the exclusive one-pion production channels, the elastic events, selected as explained above, were first removed from the 2p sample. The resulting $M^2_{miss}(\mathrm{p,p})$ spectra, shown in fig. 4a and c, are peaked close to the squared pion mass ($m^2_\pi = 0.02\,\mathrm{GeV}^2/c^4$). In the case of the p$\pi^+$ events, the distributions of the missing mass to the pπ^+ system ($M_{miss}(\mathrm{p},\pi^+)$) are shown in fig. 4b, and the unmeasured neutrons become visible as peaks around $0.94\,\mathrm{GeV}/c^2$. The contribution of two-pion production is seen on the right-hand side of the peaks. At 2.2 GeV, this channel was simulated as resulting from a double Δ production, with normalization adjusted such as to fit the data at the highest missing masses, as shown in fig. 4c and d. For each phase space bin considered in the analysis, the two-pion contribution was subtracted and the remaining yield was then fitted with a function consisting of the sum of two Gaussians plus a polynomial background. The signal was defined as the yield above this background; systematic errors were of the order of 5%. For the 1.25 GeV data set, the two-pion production region was simply excluded from the fit. Systematic errors for the signal yield were estimated from a variation of the background parameterization to be of the order of 1–3%.

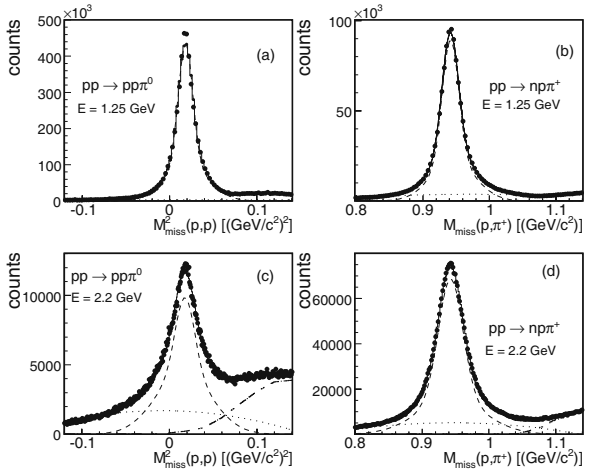

Fig. 4. Selection of events from pp → pnπ^+ and pp → ppπ^0 reactions based on a fit of missing masses. In the case of 2.2 GeV incident energy, the 2π production deduced from the simulation (dash-dotted curves) is subtracted before the fit. The fitting function consists of a sum of one polynomial (dotted curves) and two Gaussians (the sum of which is shown as dashed curves). The solid curves show the sums of all the contributions.

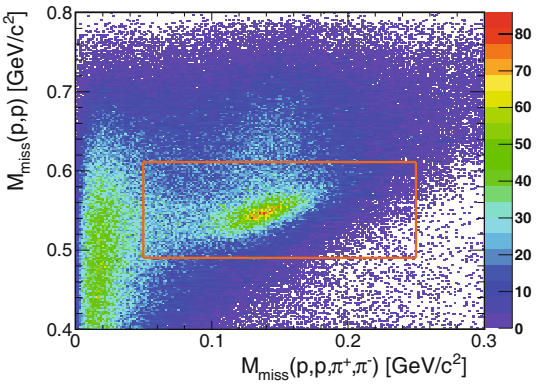

Fig. 5. (Color online) Analysis of the pp$\pi^+\pi^-$ events in the pp reaction at 2.2 GeV. The correlation between the missing mass to the two-proton system ($M_{miss}(\mathrm{p,p})$) and the missing mass to the four-particle ($M_{miss}(\mathrm{p,p},\pi^+,\pi^-)$) is shown. Events from the pp → pp$\pi^+\pi^-$ reaction are visible for $M_{miss}(\mathrm{p,p},\pi^+,\pi^-)$ close to zero. The η peak is clearly visible for $M_{miss}(\mathrm{p,p})$ around the η mass and $M^{pp\pi^+\pi^-}_{miss}$ close to the π^0 mass. The orange rectangle indicates the region used to further extract the η signal.

3.1.2 Selection of the pp → ppη → pp$\pi^+\pi^-\pi^0$ channel

To investigate the pp → ppη → pp$\pi^+\pi^-\pi^0$ channel, events with two protons, one positive and one negative pion (pp$\pi^+\pi^-$ events) are considered [54–56]. Two observables have been defined: the missing masses M_{miss} (p,p) and $M_{miss}(\mathrm{p,p},\pi^+,\pi^-)$ to the two-proton and four-particle systems, respectively. The correlation between these two missing masses is displayed in fig. 5. The concentration of events with a missing mass to the pp$\pi^+\pi^-$ system slightly above zero is due to the pp → pp$\pi^+\pi^-$ reaction; the broad structure with

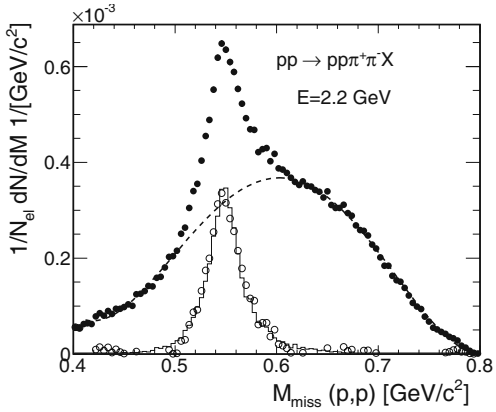

Fig. 6. Distribution of the missing mass to the two-proton system ($M_{miss}(\mathrm{p,p})$) for the $\mathrm{pp}\pi^+\pi^-$ events measured in the pp reaction at 2.2 GeV, after selection on the missing mass to the four-particle syatem ($M_{miss}(\mathrm{p,p},\pi^+,\pi^-)$) around the π^0 mass (full black dots). The data are normalized to the pp elastic yield. The dashed curve shows the fit of the non resonant three-pion background. The empty circles result from the subtraction of this background and define the η signal. The full histogram is the result of the simulation of the $\mathrm{pp} \to \mathrm{pp}\eta$ reaction.

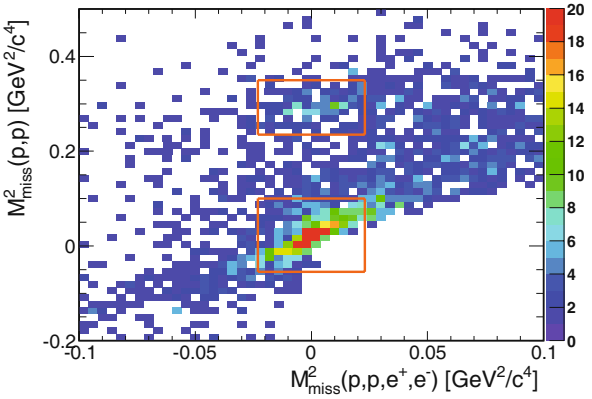

Fig. 7. (Color online) Analysis of the $\mathrm{ppe^+e^-}$ events in the pp reaction at 2.2 GeV. Correlation between the square of the missing mass to the two-proton system ($M^2_{miss}(\mathrm{p,p})$) and the square of the missing mass to the four-particle system ($M^2_{miss}(\mathrm{p,p,e^+,e^-})$) (see text). Events from the $\mathrm{pp} \to \mathrm{ppe^+e^-}\gamma$ reaction are visible for $M^2_{miss}(\mathrm{p,p,e^+,e^-})$ around zero. The orange rectangles show the limits used to extract the π^0 and η Dalitz decay signals.

$M_{miss}(\mathrm{p,p},\pi^+,\pi^-)$ around the π^0 mass corresponds to the $\mathrm{pp} \to \mathrm{pp}\pi^+\pi^-\pi^0$ final state and contains an elongated spot around $M_{miss}(\mathrm{p,p}) = 0.55\,\mathrm{GeV}/c^2$, clearly due to the $\mathrm{pp} \to \mathrm{pp}\eta$ signal. To extract the latter, first a selection of $M_{miss}(\mathrm{p,p},\pi^+,\pi^-)$ between 0.05 and 0.25 GeV/c^2, (corresponding to the vertical edges of the rectangle in fig. 5), was applied in order to reject most of the $\mathrm{pp}\pi^+\pi^-$ background.

The resulting ($M_{miss}(\mathrm{p,p})$) spectrum, normalized to the elastic yield is displayed in fig. 6 and shows a peak at the mass of the η meson on top of a broad continuum, which is mainly due to the non-resonant $\pi^+\pi^-\pi^0$ production. Its contribution in the peak region (*i.e.* missing masses between 0.490 and 0.610 GeV/c^2, delimited by the horizontal edges of the rectangle in fig. 5) was obtained from a polynomial fit of the data outside the peak region. The η signal was defined as the yield above this background, corresponding to about 24800 counts. The sensitivity to the background suppression was studied by varying the limits for the fit. It gave a systematic error of the order of ±4%. The missing-mass distribution obtained from the simulation of the $\mathrm{pp} \to \mathrm{pp}\eta$ channel is shown as a full histogram in fig. 6. Its width depends only marginally on the ingredients of the model for the η production, which will be discussed in more details in sect. 4. The agreement of simulation and experimental signal confirms the consistency of the extracted η signal and the good description of the detector resolution in the simulation.

3.2 Exclusive dielectron channels at 2.2 GeV beam energy $\mathrm{pp} \to \mathrm{pp}\pi^0/\eta \to \mathrm{ppe^+e^-}\gamma$

To reconstruct the $\mathrm{pp} \to \mathrm{pp}\pi^0/\eta \to \mathrm{ppe^+e^-}\gamma$ channels at 2.2 GeV beam energy, all events with two protons and one dielectron ($\mathrm{ppe^+e^-}$) have been selected, utilizing conversion pair rejection, as described in sect. 2.2 and [52, 55–57]. The same analysis procedure was also applied to events containing like-sign pairs ($\mathrm{ppe^+e^+}$ and $\mathrm{ppe^-e^-}$). The combinatorial background, defined as the arithmetical mean of the corresponding distributions for the latter two event samples, were then subtracted from the unlike-sign pair distributions. The signal-to-background ratios are of the order of 3 in the π^0 region and of 4 in the η region. In the same way as for the $\mathrm{pp}\pi^+\pi^-$ events, the missing-masses to the two-proton system $M_{miss}(\mathrm{p,p})$ and to the four-particle system $M_{miss}(\mathrm{p,p,e^+,e^-})$ were reconstructed, respectively.

The correlation between the squares of both missing masses is shown in fig. 7 after combinatorial background subtraction. Events from the $\mathrm{pp} \to \mathrm{ppe^+e^-}\gamma$ reaction are visible for $M^2_{miss}(\mathrm{p,p,e^+,e^-})$ around zero. The contributions from $\mathrm{pp} \to \mathrm{pp}\pi^0/\eta$ reactions followed by Dalitz decays $\pi^0/\eta \to \mathrm{e^+e^-}\gamma$ can be seen for $M^2_{miss}(\mathrm{p,p})$ close to the π^0 and η squared masses, respectively. The regions where both signals are extracted are shown as rectangles in fig. 7. The main remaining background is due to $\mathrm{e^+e^-}$ pairs from the Dalitz decay of a π^0 produced in multi-pion production processes. Its contribution, of the order of 5% has been simulated using the cross-sections 1.09 mb for $\pi^0\pi^0$ production and 0.50 mb for the $\pi^0\pi^0\pi^0$ and $\pi^0\pi^+\pi^-$ [2], and is removed bin by bin, as illustrated in fig. 8. Systematic errors of the order of 3% and 8% have been estimated for the π^0 and η signal yields, respectively, by varying the missing-mass limits and the shape of the multipion background.

A total amount of $6800 \pm 82_{stat}$ $\pi^0 \to \gamma\mathrm{e^+e^-}$ events and 235 $\pm 19_{stat}$ $\eta \to \gamma\mathrm{e^+e^-}$ events have been extracted. The dashed histogram in fig. 8 is the result of the simulation of π^0 and η Dalitz decays, with ingredients based on a resonance model, as will be explained in the following. The widths of the missing-mass peaks, which do not depend on the details of the model and mainly reflect the momentum resolution of the particle tracks, are similar to

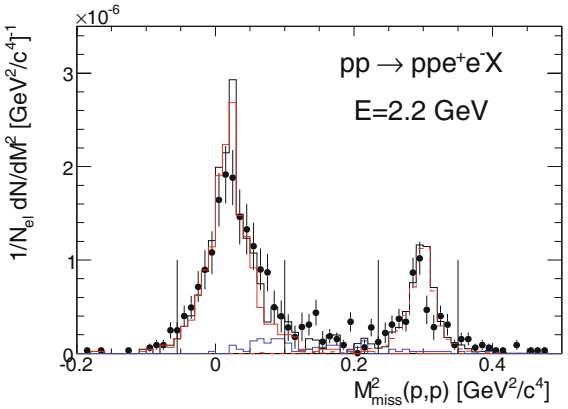

Fig. 8. (Color online) Distribution of squared missing mass to the two-proton system $M^2_{miss}(\mathrm{p,p})$ (black dots) for $\mathrm{ppe^+e^-}$ events after a cut on the missing mass to the four-particle system ($|M^2_{miss}(\mathrm{p,p,e^+,e^-})| < 0.023\,\mathrm{GeV}^2/c^4$). The yields are divided by the pp elastic scattering yield. The histograms show the results of GEANT simulations. The red histograms peaking at the π^0 and η squared masses correspond to the exclusive π^0 and η production, respectively, followed by Dalitz decay, with cross sections as listed in table 2. The blue histogram shows the contribution of multipion background, which is subtracted from the data, as explained in the text. The vertical lines depict the limits used to extract the experimental signals strength.

the experimental ones. In the same way as for the other analysis channels, this gives confidence on the reliability of the procedure to extract the proper signal selection cuts from the simulation.

4 Simulation of the reaction channels

The inputs of our simulation are inspired by the resonance model by Teis *et al.*, which is the basis for the coupled channel BUU transport code (CBUU) [31]. The contribution of $\Delta(1232)$, which is dominant for the pion production at the lowest energies, is taken from the One-Pion Exchange (OPE) model of Dmitriev *et al.* [32], which describes quite well the measured cross-sections, invariant-mass distributions, and angular distributions of the pp $\rightarrow$ pnπ^+ reaction at incident energies between 0.97 and 3.2 GeV [3,4,18]. One important parameter of the model, which had been fitted to reproduce these data, is the cut-off parameter $\Lambda_\pi = 0.63\,\mathrm{GeV}$, entering the $\pi\mathrm{N}\Delta$ and πNN vertex form factor

$$F(t) = \frac{\Lambda_\pi^2 - m_\pi^2}{\Lambda_\pi^2 - t}\,,$$

with t being the four-momentum transfer squared and m_π the pion mass. The available cross-section values for exclusive one-pion, two-pion or η production in pp and pn reactions were used to fit the contributions of isospin 1/2 (N*) and isospin 3/2 resonances other than the $\Delta(1232)$ [31].

For the simulation of the channels analysed in our experiment, we employed the event generator PLUTO [50] and included in its data base the cross-sections for the different reactions (see table 2). The cross-sections in the two first columns are directly taken from [31] and the ones in the last columns are adjusted to better describe the present data, as will be shown in sect. 5. The following relations derived from the isospin coefficients, are fulfilled in the simulation:

$$\sigma(\mathrm{pp} \rightarrow \Delta^{++}\mathrm{n} \rightarrow \pi^+\mathrm{pn}) = 9\sigma(\mathrm{pp} \rightarrow \Delta^+\mathrm{p} \rightarrow \pi^+\mathrm{np}), \quad (3)$$

$$= \frac{9}{2}\sigma(\mathrm{pp} \rightarrow \Delta^+\mathrm{p} \rightarrow \pi^0\mathrm{pp}), \quad (4)$$

$$\sigma(\mathrm{pp} \rightarrow \Delta\mathrm{N} \rightarrow \pi^+\mathrm{pn}) = 5\sigma(\mathrm{pp} \rightarrow \Delta^+\mathrm{p} \rightarrow \pi^0\mathrm{pp}). \quad (5)$$

In the same way, one gets for the $I = 1/2$ resonances,

$$\sigma(\mathrm{pp} \rightarrow \mathrm{N}^\star\mathrm{p} \rightarrow \pi^+\mathrm{np}) = 2\sigma(\mathrm{pp} \rightarrow \mathrm{N}^\star\mathrm{p} \rightarrow \pi^0\mathrm{pp}).$$

Resonances heavier than N(1535), which, in the original Teis fit [31], contribute 7% and 11% to the pnπ^+ and ppπ^0 final states, are neglected in our approach. As described in more detail in [50], the resonance mass distributions were taken according to [31]. Besides the already mentioned case of the $\Delta(1232)$, the angular distributions for the production of the other resonances are assumed to be isotropic in the pp center-of-mass frame, as in the original Teis model [31], except for the N(1440) resonance, where a steep distribution following the One-Boson Exchange (OBE) model of [59] was implemented. The decay angular distributions were kept isotropic, as in [31], except for the $\Delta(1232)$. In this case, the angular distribution of the

Table 2. Cross-sections used in the simulation. Elastic pp cross-sections taken from [49] and [58] are used for the normalisation of the measurements. For the inelastic channels, the first set of cross-sections (σ_{Teis}) is taken from [31] and is used in model A (see sect. 4) at both energies and in model B (see sect. 5.2.2) at 1.25 GeV. For the η production, the ratio of N*(1535) to non-resonant production is taken from DISTO [30]. The second set (σ_{adj}), used in model B at 2.2 GeV, is adjusted to the HADES data (see text).

Final state	Intermediate process	σ_{Teis} (mb) [31]		σ_{adj} (mb)
		1.25 GeV	2.2 GeV	2.2 GeV
pp	pp elastic	23.5	17.8	–
pnπ^+	pp $\rightarrow \Delta^{++}(1232)$ n	16.80	10.80	10.80
	pp $\rightarrow \Delta^{+}(1232)$ p	1.87	1.20	1.20
	pp $\rightarrow$ N*(1440) p	0.30	0.82	1.60
	pp $\rightarrow$ N*(1520) p	0	0.18	0.36
	pp $\rightarrow$ N*(1535) p	0	0.19	0.64
	Non-resonant	0	0	0.30
	Total	18.97	13.09	14.90
ppπ^0	pp $\rightarrow \Delta^{+}(1232)$ p	3.73	2.40	2.40
	pp $\rightarrow$ N*(1440) p	0.15	0.41	0.80
	pp $\rightarrow$ N*(1520) p	0	0.09	0.18
	pp $\rightarrow$ N*(1535) p	0	0.10	0.32
	Non-resonant	0	0	0.15
	Total	3.88	2.99	3.85
pp $\rightarrow$ ppη	pp $\rightarrow$ N*(1535) p	0	0.0725	0.082
	Non-resonant	0	0.0525	0.060
	Total	0	0.125	0.142

Table 3. Summary of the modifications introduced in models A and B with respect to the resonance model [31] (see text for more details). (1): pp and pn final-state interaction, anisotropic $\Delta(1232)$ decay angular distribution, N(1440) production angular distribution from [59]. (2): Λ_π cut-off parameter changed from 0.63 GeV to 0.75 GeV and $\Delta(1232)$ production angular distribution further adjusted to describe the neutron angular distribution in the pp $\rightarrow$ pnπ^+ channel. (3) change of production cross-sections for N(1440), N(1520) and N(1535) resonances and introduction of a non-resonant contribution following table 2.

	Model A	Model B
1.25 GeV	(1)	(1) and (2)
2.2 GeV	(1)	(1) and (3)

Δ decay ($\Delta \rightarrow$ Nπ) behaves as $1 + 0.65\ \cos^2\theta$, where θ is the angle between the π momentum in the Δ rest frame and the momentum transfer calculated in the rest frame of the excited nucleon. Such a shape was indeed found to reproduce the available data [5,8].

For the η production, a non-resonant contribution was introduced, in addition to the N(1535) (see table 2) with the same proportion as in the analysis of the DISTO data [30], measured at similar beam energies, and was simulated following phase-space distributions. For both resonant and non-resonant contributions, the angular distribution was deduced from the DISTO data. The η production cross-section, which was not measured in the DISTO experiment, is taken from [31]. The description of the Dalitz decay of η and π^0 mesons uses Vector Meson Dominance (VMD) model form factors (cf. [50]).

Finally, the pp and pn final-state interactions have been implemented using the Jost function to weight the distributions in the simulation [60]. This model, including the changes with respect to the original resonance model [31] mentionned above and summarized in table 3 is called "model A" in the following. In the course of the paper, a second model ("model B") will be introduced, which consists in a better parameterization of the measured data.

5 Results and comparison with resonance model

5.1 Dominance of Δ resonance in one-pion production channels

After selecting events from the one-pion production channels, following the procedure described in sect. 3.1.1, we first investigate the Dalitz plots (fig. 9) with respect to the footprints of a resonant behaviour of particle production. For the ppπ^0 channel, an accumulation of yield for $M^2_{inv}(\mathrm{p},\pi^0) = 1.5\,(\mathrm{GeV}/c^2)^2$, corresponding to the excitation of the Δ^+ resonance is clearly seen at both incident energies.

For the pp $\rightarrow$ pnπ^+ reaction, the Δ^{++} signal stands out markedly at $M^2_{inv}(\mathrm{p},\pi^+) = 1.5\,(\mathrm{GeV}/c^2)^2$, while the Δ^+ signal located at $M^2_{inv}(\mathrm{n},\pi^+) = 1.5\,(\mathrm{GeV}/c^2)^2$ is not

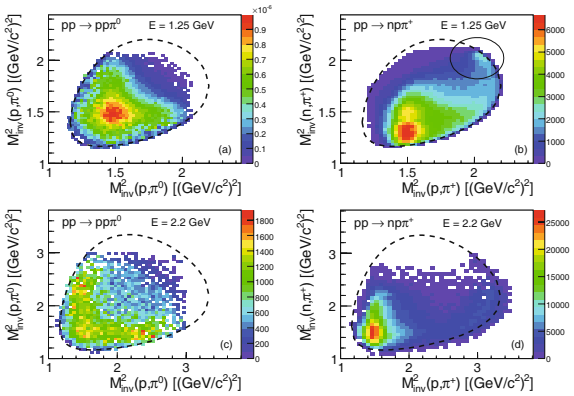

Fig. 9. (Color online) Dalitz plots of the pp $\rightarrow$ ppπ^0 (left panels) and pp $\rightarrow$ pnπ^+ (right panels) reactions: nπ^+ and pπ^0 invariant-mass-squared distributions at 1.25 GeV (upper row) and 2.2 GeV (lower row). In panel (c), the region affected by the final-state interaction of the reaction pp $\rightarrow$ pnπ^+ is marked by a circle.

visible. The dashed curves in fig. 9 indicate the kinematical limits of the Dalitz plot for the different channels. The empty zones in the plots are due to the acceptance cuts, the dominant effect being due to the minimum proton polar detection angle of about 18°. For the pp $\rightarrow$ pnπ^+ reaction at 1.25 GeV, the enhanced population for both $M^2_{inv}(\mathrm{p},\pi^+)$ and $M^2_{inv}(\mathrm{n},\pi^+)$ around $2\,(\mathrm{GeV}/c^2)^2$ is due to the pn Final-State Interaction (FSI), which enhances events with small relative momentum between the proton and the neutron. The FSI is less apparent in the pnπ^+ channel at 2.2 GeV, since it affects events with proton angles below the acceptance limit. For the ppπ^0 channel, the pp FSI has a maximum effect when both protons hit the same sector of the HADES detector, which is suppressed by the trigger configuration.

Figure 10 exhibits, respectively, the pπ^0 invariant mass for the pp $\rightarrow$ ppπ^0 reaction in the left part and the pπ^+ and nπ^+ invariant masses for the pp $\rightarrow$ pnπ^+ reaction in the right part. The data are corrected for reconstruction efficiencies and normalized using the total pp elastic cross-section, as explained in sects. 2.3 and 2.4. Error bars include statistical and systematic errors due to signal selection (1–5%) and efficiency corrections (5–10%). In addition, both isospin channels at a given energy are affected by the same global normalisation uncertainty of the order of 6% at 1.25 GeV and 11% at 2.2 GeV. The $M_{inv}(\mathrm{p},\pi^+)$ and $M_{inv}(\mathrm{p},\pi^0)$ distributions are peaked around $1.23\,\mathrm{GeV}/c^2$, which confirms that most of the pions are produced via Δ decay, although the distributions are obviously distorted by the acceptance. The different contributions of the simulation with cross-sections taken from [31] are shown in fig. 10, too. At both energies, the $M_{inv}(\mathrm{p},\pi^+)$ and $M_{inv}(\mathrm{p},\pi^0)$ distributions are mainly sensitive to the Δ contributions. The trend of the data is rather well reproduced, although obvious discrepancies concerning both the yields and the shapes can be observed.

At 1.25 GeV, the model A overestimates the experimental yield by 20% for pnπ^+ and underestimates it by 20% for ppπ^0. For the pnπ^+ channel, this discrepancy

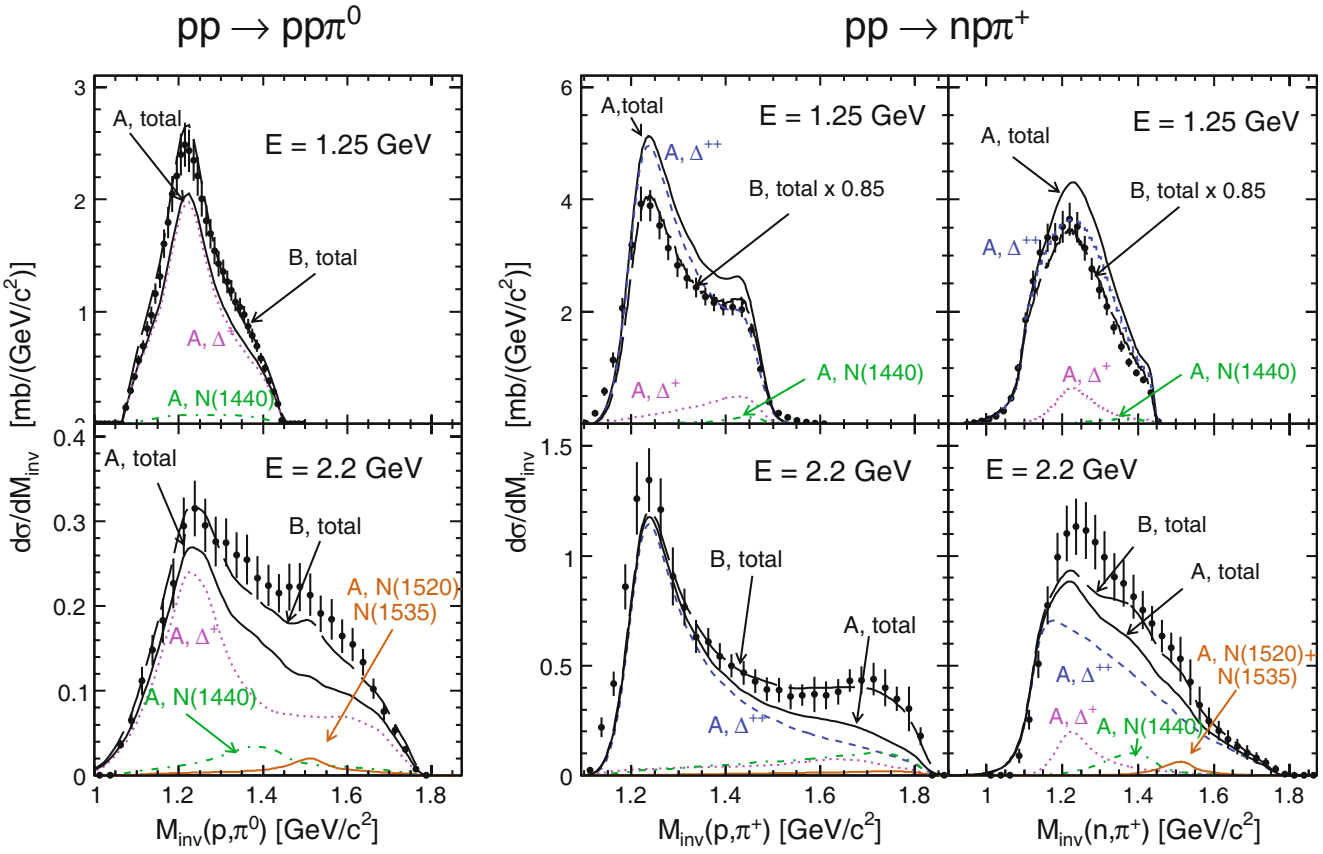

Fig. 10. (Color online) πN invariant-mass distributions (full dots) measured in pp → ppπ^0 and pp → pnπ$^+$ reactions at 1.25 GeV (top row) and 2.2 GeV (bottom row). The data are compared inside the detector acceptance on an absolute scale to the predictions of the model A (see sect. 4) with contributions of $\Delta^+(1232)$ (pink dotted curve), $\Delta^{++}(1232)$ (dashed blue curve), N(1440) (green short dash-dotted curve) and N(1520) + N(1535) (long dash-dotted light brown curve). The long dashed curve shows the result of the model B with a scaling factor of 0.85 applied in the case of pp → pnπ$^+$ at 1.25 GeV (see sect. 5.2.2).

is slightly larger than expected by taking into account, on the one hand, the discrepancies of the fit to previous data in both isospin channels and, on the other hand, the combined uncertainty of normalisation (about ±7%) and global efficiciency corrections (about ±8%). However, the yields are obtained here in a limited region of the phase space, and they are therefore sensitive to the distributions used in the model, as will be shown in the following.

At 2.2 GeV, the contributions of higher-lying resonances clearly show up at high invariant masses and are underestimated in the simulation using the cross-sections from [31] (see table 2).

5.2 Analysis of the pp → pnπ$^+$ channel

We shall now discuss in some detail the distributions obtained in the different channels. The results are first compared to the resonance model [31] to show its capability to describe the data and then a better parameterization of the data is proposed.

5.2.1 Δ resonance angular distributions

The neutron angular distributions in the center-of-mass system measured in the pp → pnπ$^+$ channel at both energies are displayed in fig. 11. These distributions mainly reflect the angular distribution of Δ resonance production, since pp→ nΔ^{++} is the dominant process for the exclusive π$^+$ production. They are strongly forward/backward peaked, as expected for the characteristic peripheral production of the Δ resonance. The distribution in fig. 11a (pp → pnπ$^+$ at 1.25 GeV) is highly distorted in the backward hemisphere, which is mainly due to the limited acceptance for protons at small laboratory angles ($\theta < 18°$). At 2.2 GeV (fig. 11b), these acceptance losses are even larger. Therefore, we did not use the backward hemisphere at this energy. We included into fig. 11 the results from the simulations. In order to compare the shapes of the neutron angle distributions, the simulations were rescaled to reproduce the integrated experimental yields. At 1.25 GeV, it can be seen that the forward/backward asymmetry is quite well reproduced by the simulation. The distribution is somewhat less peaked in the case of the Δ$^+$ and N* excitations, since the neutron comes from the decay of the resonance. The Δ^{++} contribution however still dominates by an order of magnitude around $\cos\theta_n$=0. The slope at forward angles is well described by the sum of the different components (solid curve), but the experimental distribution is slightly less steep than the simulated one, at

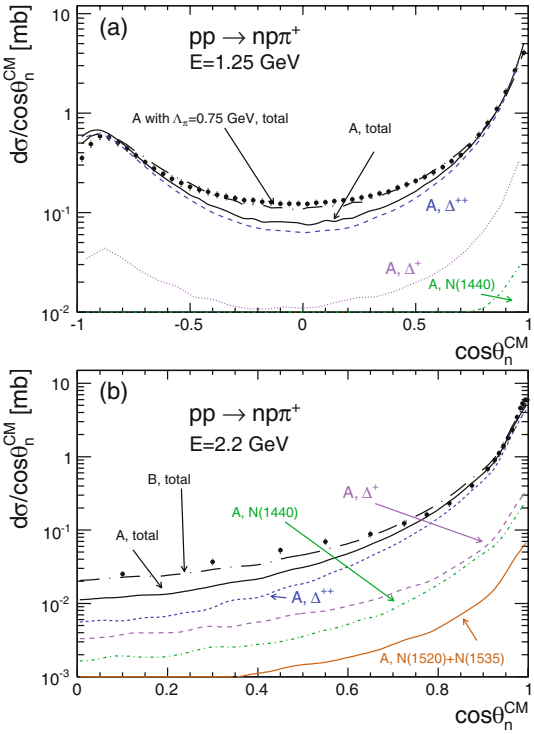

Fig. 11. (Color online) Angular distributions of the neutron in the pp center-of-mass system. Top: $E = 1.25\,\text{GeV}$, Bottom: $E = 2.2\,\text{GeV}$. Data (black points) are compared to simulations with model A (solid curve) including Δ^{++} (blue dashed curve), Δ^{+} (pink dotted curve), N(1440) (green dash-dotted curve), N(1520) and N(1535) (brown dot-dot-dashed curve). The dot-dashed curves show the result of model A with $\Lambda_\pi = 0.75\,\text{GeV}$ in the case of 1.25 GeV and model B in the case of 2.2 GeV. Both calculations are scaled to reproduce the respective integrated experimental yield.

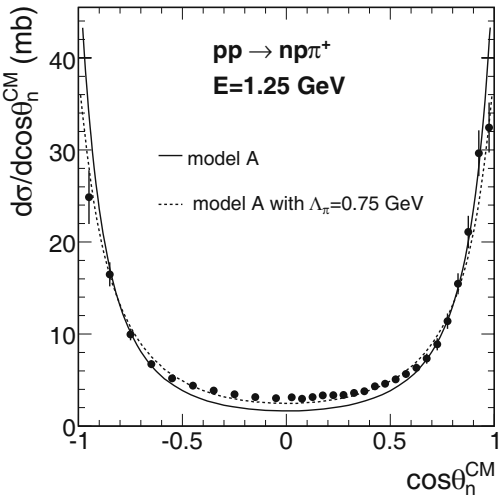

Fig. 12. Angular distribution of neutron in center-of-mass system after acceptance correction for the pp → pnπ+ reaction at 1.25 GeV. Data (black points) are compared to simulations based on model A with $\Lambda_\pi = 0.63\,\text{GeV}$ (solid curve) and the modified version with $\Lambda_\pi = 0.75\,\text{GeV}$ (dashed curve). Both simulation curves are normalized to reproduce the integrated experimental yield.

both energies. With the chosen normalisation to the integrated yield, the experimental yield at $\cos\theta_n = 0$ is larger than the simulated one by factors of about 1.6 and 2.5 at 1.25 GeV and 2.2 GeV, respectively.

Acceptance-corrected angular distributions, which are useful to provide a result independent of the detector geometry, can only be obtained using a model. This could be done with a good precision, at 1.25 GeV only, where the reaction mechanism is best under control, due to the overwhelming contribution of the Δ resonance. The acceptance correction factors are calculated for different ($\cos\theta_n$, $M_{inv}(\text{p},\pi^+)$) cells, chosen to optimize the precision of the correction and defined as the ratio of events from simulation in full phase space and in geometrical HADES acceptance. In this way, the factors depend weakly on how the invariant mass and angular distributions of the Δ are realized in the model. Remaining uncertainties come mainly from the decay angle distribution of the Δ resonance. Due to the limited acceptance of our experiment, the measured distributions of the π^+ emission angle do not allow to improve the results from previous measurements [5,8], in which a decay angle distribution compatible with $1 + B\cos^2\theta$ with $B = 0.65 \pm 0.30$, was measured. The uncertainty on this anisotropy parameter has therefore been taken into account to calculate the systematic errors. The acceptance-corrected neutron angular distribution obtained in this way is shown with statistical and systematic errors in fig. 12. Once corrected for acceptance, the neutron angular distribution recovers the expected forward/backward symmetry. The integral of this distribution gives the cross-section for the pp → pnπ+ reaction, as will be discussed in sect. 5.4. The prediction from the resonance model is also shown, on fig. 12, after a renormalization by a factor 0.85 to match the integrated yield of the experimental data. The underestimation of the experimental yield around $\cos\theta_n \approx 0$ is consistent with the result obtained within the HADES acceptance.

Since the shape of the Δ production angular distribution in the OPE model depends on the value of the cut-off parameter Λ_π, the sensitivity of the simulation to this parameter was studied, keeping the cross-sections of the different contributions as in [31]. For $\Lambda_\pi = 0.75\,\text{GeV}$, instead of the standard value of 0.63 GeV, the difference between model and experimental data at $\cos\theta_n = 0$ is reduced from 40% to about 15% (see figs. 11a and 12). It is clear, however, that the discrepancy of the measured angular distributions with respect to the OPE model might have a different origin than just a refitting of the cut-off parameter. In the region of $\cos\theta_n = 0$, ρ meson exchange could be more important due to the higher four-momentum transfer. In addition, non-resonant contributions might have a much flatter angular distribution than the Δ contribution. Finally, the interference between the amplitudes of the different resonances are neglected in our description.

5.2.2 Modifications of the resonance model

Considering the aforementioned deviations of the experimental distributions with respect to the resonance model

of [31], some modifications were introduced to provide a better parameterization of the data.

At 2.2 GeV, the Δ resonance contributions were not changed, but the cross-sections of higher-lying resonances (N(1440), N(1520) and N(1535)) were increased and a non-resonant contribution, generated with a phase-space distribution, was added. The new cross-sections are listed in the last column of table 2. A better description of the $p\pi^+$ and π^+n invariant mass distributions in fig. 10 and of the neutron angular distribution in fig. 11 in the $pn\pi^+$ channel can be obtained, as can be seen by the long dash-dotted curves on the corresponding pictures.

At 1.25 GeV, we have chosen to keep the cross-sections of [31], but, in order to provide a parameterization of the data yet more precise than the OPE model with $\Lambda_\pi = 0.75$ GeV (see sect. 5.2.1), an iterative procedure was used to fit the Δ production angular distribution such as to reproduce the measured neutron angular distribution. Due to the dominance of the Δ^{++} excitation in the $pp \to pn\pi^+$ reaction, this angular distribution is very close to the neutron angular distribution presented in fig. 12.

Applying an overall normalisation factor of 0.85, which is consistent with the different errors (see sect. 5.4), the yields and shapes of the invariant-mass spectra are well described by this modified resonance model, as can be seen by the long dashed curve in fig. 10. Besides, the pn FSI, introduced already in model A, while affecting only a very small fraction of the events, is found important to reproduce the behaviour of the distribution for the highest invariant masses. In this way, a new parameterization of the data is proposed at both energies, called "model B". The modifications with respect to model A are summarized in table 3. This parameterization will be checked for the $pp \to pp\pi^0$ channel in sect. 5.3, while, in the next section, the invariant masses measured at 1.25 GeV are presented in more detail.

5.2.3 Invariant-mass distributions at 1.25 GeV

To further understand the contributing mechanisms in their impact on the neutron angle $\cos\theta_n$, the $p\pi^+$ and π^+n invariant-mass spectra were studied in the forward hemisphere in five different $\cos\theta_n$ bins, as shown in figs. 13 and 14. The spectra are compared to the results of the simulation with model B, which takes into account the experimental neutron angle distribution (see sect. 5.2.2). As before, the model B is scaled by a factor 0.85 to reproduce the experimental yield integrated over the neutron angle. The evolution of the shapes of the invariant-mass spectra as a function of neutron angle in the simulation is mainly due to the detector acceptance and trigger effects on the dominant Δ^{++} contribution. In particular, the structure at about 1.45 GeV for $\cos\theta_n < 0.8$ is due to the requirement for the pion and proton to hit two opposite sectors. Although discrepancies of the order of 25% can be observed, the experimental spectra are rather well reproduced. In particular, the shape of the $p\pi^+$ invariant-mass distribution around $\cos\theta_n = 0$ seems to indicate that the Δ contribution is still dominant in this region.

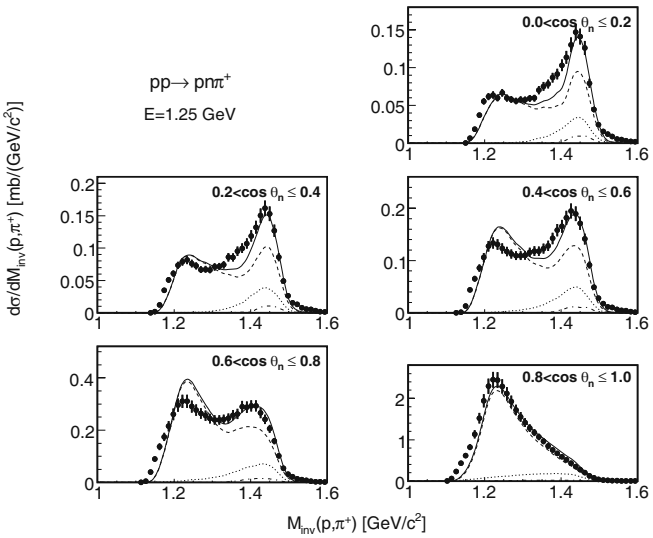

Fig. 13. $p\pi^+$ invariant-mass distributions measured in $pp \to pn\pi^+$ reactions at 1.25 GeV for different bins in $\cos\theta_n$ (full dots), compared to model B (see text) rescaled by a factor 0.85, with total (full curves), $\Delta^{++}(1232)$ (dashed curves), $\Delta^{+}(1232)$ (dotted curves), and N(1440) (dash-dotted curves) contributions.

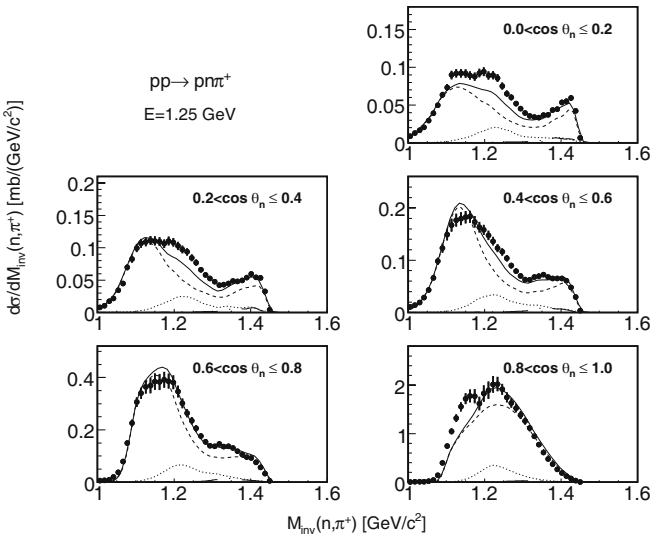

Fig. 14. Same as fig. 13, but for for π^+n invariant-mass distributions.

The introduced flattening of the angular distribution of the Δ production both compensates the missing yield around $\cos\theta_n = 0$ in the original model and gives better agreement of the invariant mass spectra. These distributions definitely contain rich information about the pion production mechanism and should be compared to more sophisticated models including interference effects and non-resonant contribution. Thanks to the high statistics, these detailed distributions can indeed provide constraints which are complementary to the results from the bubble chamber experiments [3,4].

5.3 Analysis of the pp → ppπ^0 channel

We will now discuss the results obtained in the ppπ^0 channel and compare them to the resonance model in its standard and modified versions.

5.3.1 Invariant masses

As mentioned in sect. 5.1, model A, based mainly on the Teis resonance model [31], underestimates the yield in the ppπ^0 channel by 20% at 1.25 GeV and 35% at 2.2 GeV (see fig. 10). After the inclusion of the changes in the model B motivated by the study of the pp → pnπ^+ channel (see sect. 5.2.2), *i.e.* a slight rescaling of the cross-sections of the different channels and the use of a phenomenological angular distribution for the Δ production, both the yields and the shapes of the π^0p invariant-mass distribution are better reproduced, as demonstrated by the long dash-dotted curves in fig. 10.

At 1.25 GeV, the change of the Δ production angular distribution in the model mainly results in a global increase of the cross-sections in the HADES acceptance by 33%, with small effect on the shape of the π^0p invariant-mass distribution. Note that, contrary to the pnπ^+ channel, no rescaling is applied to the model. In contrast to the pp → pnπ^+ case, where the whole Δ production angular distribution could be measured, Δ production in forward or backward angles is suppressed by the HADES acceptance in the pp → ppπ^0 channel. This is the reason of the higher yield obtained for the simulation with model B, where the Δ production angular distribution is flatter.

At 2.2 GeV, the change of the shape of the π^0p invariant-mass distribution is induced by the increase of the cross-sections for the higher-lying resonances (N*(1440), N*(1520), N*(1535)) and the introduction of a non-resonant contribution.

To summarize, the changes motivated by the study of the analysis of the pp → pnπ^+ channel also improve the description of the yields in the pp → ppπ^0 channel, which adds consistency to the procedure. To complete the study, the proton angular distributions measured at 1.25 GeV are investigated in the next section.

5.3.2 Proton angular distributions at 1.25 GeV

Even at 1.25 GeV, where pp → pΔ is the dominant process, the Δ^+ resonance cannot be unambiguously reconstructed due to the two protons in the exit channel. However, although both, the proton coming from the decay of the Δ resonance and the scattered one, contribute, the shape of their angular distribution inside the HADES acceptance is mainly sensitive to the distribution of Δ^+ production angle and depends only marginally on the decay angle in our simple two-step model. It is therefore interesting to check whether the distribution of the proton angle allows to draw conclusions on the distribution of the Δ angle, which are consistent with the pnπ^+ channel. As

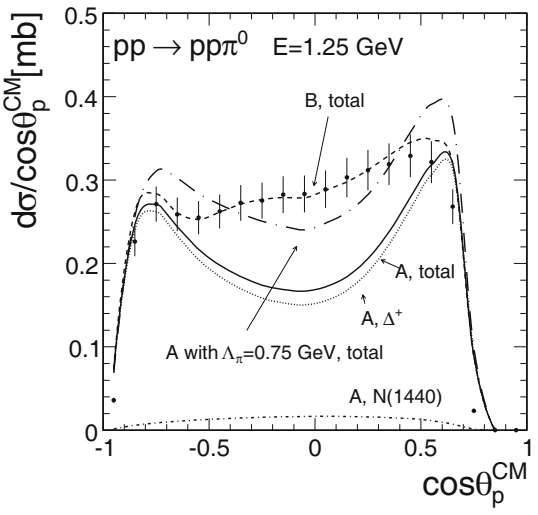

Fig. 15. Center-of-mass proton angular distribution in the reaction pp → ppπ^0 at 1.25 GeV compared to three versions of the resonance model: model A (full curve), modified version of model A with $\Lambda_\pi = 0.75$ GeV (long dot-dashed curve), and model B (dashed curve). The Δ^+ and N*(1440) contributions are depicted separately for model A by dotted and short dot-dashed curves, respectively.

can be seen in fig. 15, the acceptance is limited to intermediate proton angles (about $45° < \theta_p^{CM} < 155°$) in the center of mass. The experimental distribution is however clearly much flatter than predicted by the simulation based on the resonance model A (see sect. 4). Changing the Λ_π parameter in the vertex form factor from 0.63 to 0.75 GeV, as motivated by the analysis of the pp → pnπ^+ reaction, the simulation comes closer to the data, although the yield around $\cos\theta_p = 0$ is still too low. This is related to the remaining underestimation of the $\cos\theta_n$ distribution in the pp → pnπ^+ channel. A better agreement can indeed be obtained with model B, which uses as an input for the Δ production angular distribution the distribution fitted to the measurement in the pp → pnπ^+ channel (see sect. 5.2.1), as shown by the dashed curve in the picture. This confirms that the two isospin channels can be described consistently with the same Δ production angular distribution. Thus, model B can be exploited for the analysis of the exclusive pp → ppe^+e^- channel at 1.25 GeV, where a realistic model for the pp → pΔ^+ reaction is needed.

5.4 Exclusive one-pion and one-eta production cross-sections

The cross sections for the different one-meson production channels are reported in the first row of table 4. For the pp → pnπ^+ channel at 1.25 GeV, the cross-section was obtained by integrating over $\cos\theta_n$ the acceptance corrected neutron angular distribution (see sect. 5.2.1). For the other channels, the modified resonance model (model B) was used to extrapolate the measured yields to 4π. More precisely, the acceptance factors were calculated as

Table 4. Cross-sections for exclusive meson production channels measured by HADES in hadronic channels are given with the total error, calculated as the quadratic sum of the statistic and systematic errors listed in the following rows.

Reaction	$pp \to pn\pi^+$		$pp \to pp\pi^0$		$pp \to pp\eta$
Energy	1.25 GeV	2.2 GeV	1.25 GeV	2.2 GeV	2.2 GeV
Cross-section (mb)	17.1 ± 2.0	14.45 ± 3.2	3.74 ± 0.48	4.15 ± 0.85	0.142 ± 0.022
Acceptance corrections	± 1.0	± 1.1	± 0.2	± 0.2	± 0.006
Normalization	± 1.1	± 1.6	± 0.25	± 0.46	± 0.016
Efficiency	± 1.3	± 2.5	± 0.33	± 0.65	± 0.013
Event selection	± 0.3	± 0.7	± 0.12	± 0.2	± 0.005
Statistics	± 0.01	± 0.01	± 0.003	± 0.004	± 0.002

a ratio of the number of events generated in the simulation to the number of events after filtering by the HADES geometrical acceptance and analysis cuts. To estimate the model dependence of these corrections, parameters of the model were varied, especially the Δ decay angular distribution for the pion production channels and the proportion of resonant contribution in the case of the η production channel. The corresponding numbers are indicated in the second row of table 4. The main sources of errors are the model dependence of the acceptance corrections (second row), the normalization procedure (third row) and the efficiency corrections (fourth row). The errors due to the event selection, following the procedures discussed in sects. 3.1.1 and 3.1.2 are also indicated (fifth row). Statistical errors (sixth row) are negligible. Note that the contribution of the error on the η branching ratio into 3 pions is also of the order of 1%. The obtained cross-section values are compatible with previous measurements, as can be seen from fig. 16.

For the pion production channels, most of the data points obtained for $\sqrt{s}$ between 2.0 and 2.4 GeV come from KEK [7] (black dots) and were not included in the Teis fits, which were based on CERN data tables [2]. For the π^+ production, the KEK points [7] fit rather well with the Teis curve as well as with previous data [4,16], while they are about 15–20% higher for the π^0 production. Our data are compatible with the Teis curve, despite a slight underestimate of the π^0 production at 2.2 GeV. As already mentioned, the relatively large error bars of our data with respect to the existing previous data are due to the combined effects of efficiency corrections, normalization and acceptance corrections, which were reduced in the case of bubble chamber experiments. The scattering of this data collection might however point to an underestimate of the error related to the event identification. From the HADES measurements, the ratios of $pp \to pn\pi^+$ to $pp \to pp\pi^0$ cross-sections 4.57 ± 0.54 at 1.25 GeV and 3.49 ± 0.63 at 2.2 GeV can be deduced, which has to be compared with the factor 5 expected in the case of Δ excitation only, see eq. (5).

As for the η production, our experiment brings a new measurement ($\sigma = 0.142 \pm 0.022$ mb) of the exclusive production cross-section in pp reaction, in a region, about

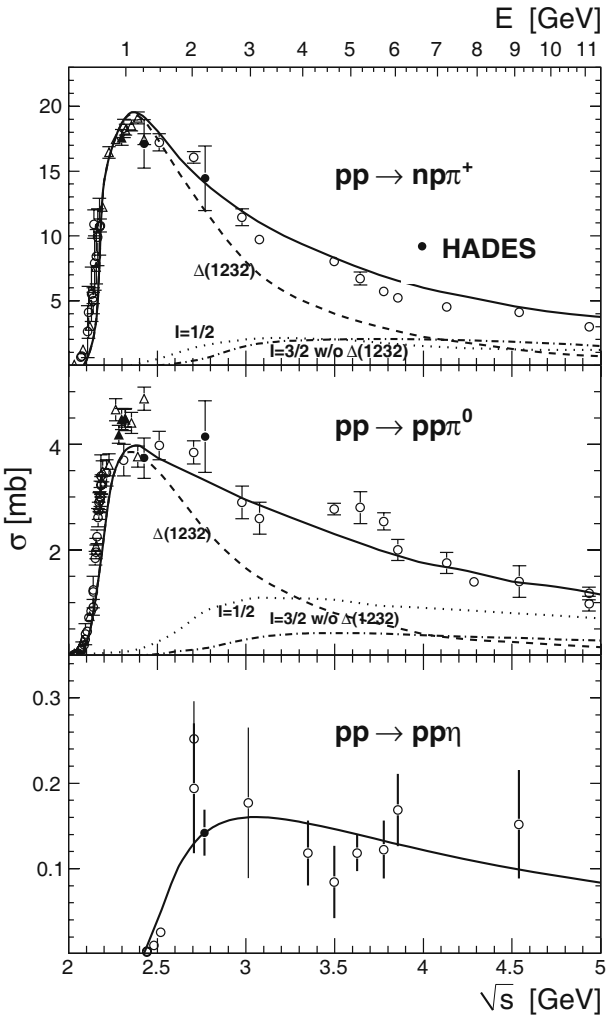

Fig. 16. Cross-sections measured by HADES (full dots) in hadronic channels for the $pp \to pn\pi^+$ (top), $pp \to pp\pi^0$ (middle) and $pp \to pp\eta$ (bottom) reactions compared to existing data (empty dots [2,20,61], empty triangles [7], full triangles [11,15]). The curves display the resonance model cross-sections [31] (total: full curve, $\Delta(1232)$: dashed curve, $I = 1/2$: dotted curve, $I = 3/2$ other than $\Delta(1232)$: dash-dotted curve).

230 MeV above the threshold, where only the two measurements from Pickup *et al.* [62] existed. Our point is in agreement with their value obtained in neutral channels, $\sigma = 0.197 \pm 0.077$ mb, while it is found below their more precise measurement obtained in the three-pion channel ($\sigma = 0.242 \pm 0.043$ mb). The quoted error might however be underestimated, as discussed in [30], considering the uncertainty due to the non-resonant background subtraction. The cross-section parameterizations used in [30] and based on fits of data with $\sqrt{s}$ ranging from threshold up to 3.4 GeV did not take into account these points and provided, at an energy of 2.2 GeV, values between 70 and 100 μb, which are much lower than both Pickup's results [62] and the value measured in the present experiment. Our measurement is in very good agreement with the resonance model [31], where the η's are assumed to be produced only via N(1535) resonance decay. This assumption of fully resonant production seems however in contradiction with the DISTO analysis [30]. Our new measurement can hence be used to test various models of η production. Previous OBE calculations [63–65] showed deviations of a factor 2 depending on the values of the ρNN*(1535) and ωNN*(1535) coupling constants, which should be updated in view of the actual constraints on these parameters, as was done recently closer to threshold [66].

5.5 π^0 and η Dalitz decay analysis

5.5.1 Dielectron invariant mass

As already explained in sect. 3.2, the π^0 and η Dalitz decay signals has been extracted, in each e^+e^- invariant-mass bin, using the missing masses to the pp and ppe^+e^- systems and were then efficiency corrected. In addition, an acceptance correction obtained from simulations with the resonance model was applied. The resulting e^+e^- invariant-mass distributions are displayed in fig. 17, with statistical errors and systematic errors added quadratically. In the case of the π^0, the largest source of systematic error is the rejection of e^+e^- pairs from photon conversion, while in the η region, it is due to e^+e^- pairs from π^0 decay in multipion production processes.

The experimental values are compared to the results of the simulation, with exclusive meson production cross-sections from table 2 and branching ratios from table 1. The good agreement obtained for both the π^0 and η peak is therefore a check of the consistent extraction of the corresponding signals, which is very useful for all dielectron analyses performed with the HADES detector. The small excess around 0.03 GeV/c^2 is most likely due to a remaining contamination of conversion pairs. The possible contribution of Dalitz decays of baryon resonances, corresponding to a ppe^+e^- final state, has also been investigated and is found to be negligible, except in the mass region close to the kinematical limit ($M_{inv}(e^+, e^-) = 0.547$ GeV/c^2), which could possibly explain that the measured yield for the reaction pp $\rightarrow$ ppη is higher than the simulation above 0.5 GeV/c^2.

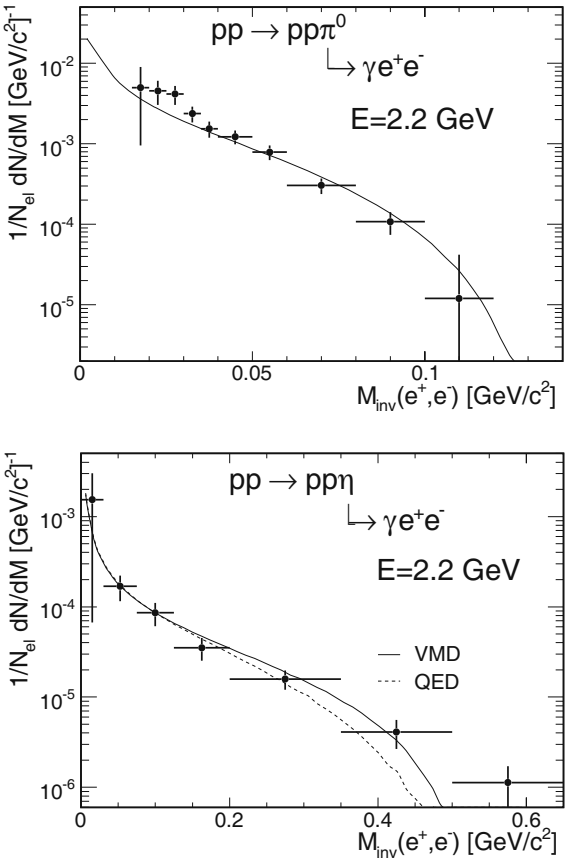

Fig. 17. Distribution of dielectron invariant masses for the π^0 (left) and η (right) Dalitz decays, obtained after efficiency and acceptance corrections and compared to the simulations with model A (full line), including VMD models. The yields have been divided by the elastic scattering yields. In the case of the η, the simulation without η form factor (labeled as QED) is shown as a dashed curve for comparison.

It has been checked that the shapes of these spectra do not depend on the ingredients of the simulation related to the meson production mechanisms, like the relative yields of the different resonant contributions, but are characteristic of their Dalitz decay. The description of these Dalitz decay processes in the simulation implies electromagnetic form factors which can be implemented in the simulation following the VMD model [50,67]. Modelling the transitions as point-like (refered to as QED) or using VMD form factors lead to negligible differences for the $\pi^0 \rightarrow \gamma e^+e^-$ case and show up for the $\eta \rightarrow \gamma e^+e^-$ case only at larger values of the e^+e^- invariant mass. There, our data are however not precise enough to provide any further quantitative constraint to these models.

The yields are well reproduced by the simulation with meson production cross-sections from table 2. In the case of the η production, since the cross-section is only fixed by our measurement in the hadronic channel (sect. 5.4), this shows the consistency of the hadronic and leptonic reconstructions and the good control of the corresponding efficiencies. More quantitatively, the ratio of yields

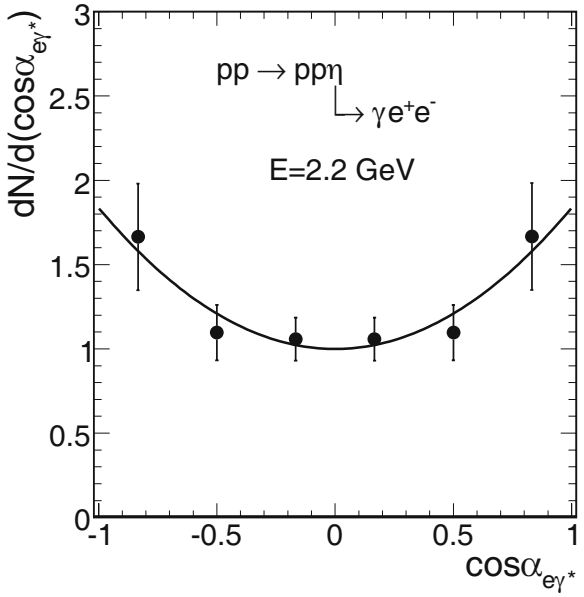

Fig. 18. Angular distributions of electrons and positrons in the virtual photon rest frame (helicity) after acceptance and efficiency correction, using an arbitrary normalization. The solid curve is the fit using $(a(1 + b\cos^2 \alpha_{e\gamma^\star}))$ with $b = 0.98 \pm 0.48$.

measured in $\pi^+\pi^-\pi^0$ and γe^+e^- decays of the η meson is 218 ± 25, *i.e.* fully consistent with the value 230 ± 5 given by the simulation. In the case of the π^0, where the production cross-sections are constrained by independent data, the analysis of the $\pi^0 \to \gamma e^+e^-$ channel provides a global consistency check of the whole analysis chain for dileptons.

5.5.2 Helicity angle

An interesting feature of the Dalitz decay of pseudo-scalar mesons is the polarization of the virtual photon which is transverse. As a consequence, the distribution of the helicity angle $\alpha_{e\gamma^\star}$ follows $1 + \cos^2 \alpha_{e\gamma^\star}$. The calculation of this angle first implies a boost of all particles in the meson rest frame. Then the helicity angle is defined as the polar angle of the electrons in the virtual photon rest frame, with respect to the virtual photon direction. The acceptance and efficiency corrections were calculated using the simulation of the dielectron production via η Dalitz decay, as described above. As shown in fig. 18, this angular distribution can be fitted by a function of the form $a(1 + b\cos^2 \alpha_{e\gamma^\star})$ with $b = 0.98 \pm 0.48$, in agreement with the QED prediction, $b = 1$ [45].

With the HADES set-up, it is therefore possible to reconstruct the helicity angle distribution of the η Dalitz decays. The extraction of the anisotropy parameter b should then be also possible in the case of the Δ Dalitz decay, where, the polarization of the virtual photon is also mainly transverse, since the Coulomb amplitude in the NΔ transition is small and hence a $1 + \cos^2 \alpha_{e\gamma^\star}$ distribution is expected. Helicity angle distributions have also been investigated in heavy-ion reactions [42] in order to identify the nature of the "excess" beyond the η contribution.

6 Summary and outlook

HADES has provided a measurement of the reactions $pp \to pn\pi^+$ and $pp \to pp\pi^0$ at 1.25 GeV and 2.2 GeV and $pp \to pp\eta$ at 2.2 GeV using both hadronic and leptonic channels. Using the hadronic channels, high statistics differential cross-sections could be measured in the HADES acceptance. In addition, integrated cross-sections were extracted for all these channels and the neutron angular distribution in the $pp \to pn\pi^+$ reaction at 1.25 GeV was fully reconstructed. These data allow to test pion production mechanisms and the contribution of baryonic resonances with a high statistical precision, in complement to previous low-statistics but high-acceptance experiments. We left for further studies the comparison of these data to calculations including resonant and non-resonant contributions in a coherent way. Our aim in this paper was twofold: first, to show the sensitivity of the present data to the ingredients of the transport models used for the dielectron production, which are based on resonance models and, second, to obtain a parameterization of meson and baryon resonance production for dielectron channels analysis. Following this line, an analysis based on a resonance model [31] was presented. An overall agreement with the original model is shown, but a better description could be obtained in both isospin channels, using at 1.25 GeV a less steep angular distribution for the $\Delta(1232)$ resonance production and at 2.2 GeV an increased production cross-section for the higher-lying resonances. A precise description of the $\Delta(1232)$ production angular distribution at 1.25 GeV is especially important for the on-going analysis of the Dalitz decay of the $\Delta(1232)$ resonance using the $pp \to ppe^+e^-$ channel. On the other hand, further information on higher-lying resonances can be gained by studying two-pion production channels, which were also recently measured in the HADES experiments. The present determination of the exclusive η production cross-section is most important, as it provides the first precise measurement of the exclusive production cross-section in a region where deviating model predictions can be found.

The reconstruction of π^0 and η Dalitz decay signals presented in this paper is fully consistent with the hadronic channels, and the invariant masses and acceptance corrected helicity angle distributions are in good agreement with QED predictions. These results confirm the ability of HADES to reconstruct sensitive observables in dielectron channels, which is a very important consistency check for previous and next-coming analyses. The helicity angle was used to study dielectron sources in heavy-ion reactions [42] in different invariant-mass regions and is also used to discriminate the $\Delta(1232)$ Dalitz decay process from the pp Bremsstrahlung contribution in the on-going analysis of the exclusive ppe^+e^- channel in pp reactions at 1.25 GeV [68].

As a final conclusion, the present analysis provided important consistency checks for dielectron studies, as well as

precise results for meson production measured in hadronic channels, paving the way for further theoretical or experimental studies of exclusive dielectron and hadronic channels in elementary reactions.

The Collaboration gratefully acknowledges the support by CNRS/IN2P3 and IPN Orsay (France), by SIP JUC Cracow (Poland) (NN202 286038, NN202198639), by HZDR, Dresden (Germany) (BMBF 06DR9059D), by TU München, Garching (Germany) (MLL München, DFG EClust 153, VH-NG-330, BMBF 06MT9156 TP5, GSI TMKrue 1012), by Goethe-University, Frankfurt (Germany) (HA216/EMMI, HIC for FAIR (LOEWE), BMBF 06FY9100I, GSI F&E), by INFN (Italy), by NPI AS CR, Rez (Czech Republic) (MSMT LC07050, GAASCR IAA100480803), by USC - Santiago de Compostela (Spain) (CPAN:CSD2007-00042).

References

1. P. Moskal *et al.*, Prog. Part. Nucl. Phys. **49**, 1 (2002).
2. A. Baldini *et al.*, in *Landolt Börnstein, New Series, Group 1*, edited by H. Schopper, Vol. **12** (Springer-Verlag, Berlin, 1988).
3. D.V. Bugg *et al.*, Phys. Rev. B **133**, 1017 (1964).
4. A.M. Eisner *et al.*, Phys. Rev. B **138**, 670 (1965).
5. T.C. Bacon *et al.*, Phys. Rev. **162**, 1320 (1967).
6. J. Hudomalj-Gabitzsch *et al.*, Phys. Rev. C **18**, 2666 (1978).
7. F. Shimizu *et al.*, Nucl. Phys. A **389**, 445 (1982).
8. A.B. Wicklund *et al.*, Phys. Rev. D **35**, 2670 (1987).
9. C. Comptour *et al.*, Nucl. Phys. A **579**, 369 (1994).
10. V.P. Andreev *et al.*, Phys. Rev. C **50**, 15 (1994).
11. V.V. Sarantsev *et al.*, Eur. Phys. J. A **21**, 303 (2004).
12. S. Abd El-Samad *et al.*, Eur. Phys. J. A **30**, 443 (2006).
13. S. Abd El-Samad *et al.*, Eur. Phys. J. A **39**, 281 (2009).
14. T. Skorodko, PhD Thesis, University of Tübingen (2009).
15. K.N. Ermakov *et al.*, Eur. Phys. J. A **47**, 159 (2011).
16. W.J. Fickinger *et al.*, Phys. Rev. **125**, 2082 (1962).
17. G. Alexander *et al.*, Phys. Rev. **154**, 1284 (1967).
18. S. Coletti *et al.*, Nuovo Cimento A **49**, 479 (1967).
19. E. Chiavassa *et al.*, Phys. Lett. B **322**, 270 (1994).
20. E. Chiavassa *et al.*, Phys. Lett. B **337**, 192 (1994).
21. A.M. Bergdolt *et al.*, Phys. Rev. D **48**, R2969 (1993).
22. F. Hibou *et al.*, Phys. Lett. B **438**, 41 (1998).
23. H. Calan *et al.*, Phys. Lett. B **458**, 190 (1999).
24. E. Roderburg *et al.*, Acta Phys. Pol. B **31**, 2299 (2000).
25. P. Winter *et al.*, Phys. Lett. B **544**, 251 (2002).
26. M. Abdel-Bary *et al.*, Eur. Phys. J. A **16**, 127 (2003).
27. A. Khoukaz *et al.*, Nucl. Phys. A **663**, 565c (2000).
28. J. Smyrski *et al.*, Phys. Lett. B **474**, 182 (2000).
29. R. Czyzykiewicz *et al.*, Phys. Rev. Lett. **98**, 122003 (2007).
30. F. Balestra *et al.*, Phys. Rev. C **69**, 064003 (2004).
31. S. Teis *et al.*, Z. Phys. A **356**, 421 (1997).
32. V. Dmitriev, O. Sushkov, C. Gaarde, Nucl. Phys. A **459**, 503 (1986).
33. M. Bleicher *et al.*, J. Phys. G **25**, 1859 (1999).
34. K. Shekhter *et al.*, Phys. Rev. C **68**, 014904 (2003).
35. M. Thomere *et al.*, Phys. Rev. C **75**, 064902 (2007).
36. E. Bratkovskaya, W. Cassing, Nucl. Phys. A **807**, 214 (2008).
37. H.W. Barz *et al.*, Open Nucl. Part. Phys. J. **3**, 1 (2010).
38. K. Schmidt *et al.*, Phys. Rev. C **79**, 064908 (2009).
39. G. Agakishiev *et al.*, Phys. Rev. Lett. **98**, 052302 (2007).
40. G. Agakishiev *et al.*, Phys. Lett. B **663**, 43 (2008).
41. The HADES Collaboration (G. Agakishiev *et al.*), Phys. Lett. B **690**, 118 (2010).
42. G. Agakishiev *et al.*, Phys. Rev. C **84**, 014902 (2011).
43. G. Agakishiev *et al.*, Eur. Phys. J. A **48**, 64 (2012).
44. G. Agakishiev *et al.*, Eur. Phys. J. A **41**, 243 (2009).
45. E.L. Bratkovskaya, O.V. Teryaev, V.D. Toneev, Phys. Lett. B **348**, 283 (1995).
46. R. Arnaldi *et al.*, Phys. Rev. Lett. **102**, 222301 (2009).
47. G. Agakishiev *et al.*, Eur. Phys. J. A **40**, 45 (2009).
48. G. Agakishiev *et al.*, Phys. Rev. C **80**, 025209 (2009).
49. D. Albers *et al.*, Eur. Phys. J. A **22**, 125 (2004).
50. I. Fröhlich *et al.*, PoS **ACAT2007**, 076 (2007) arXiv: 0708.2382v2.
51. I. Fröhlich *et al.*, Eur. Phys. J. A **45**, 401 (2010).
52. M. Wisniowski, PhD Thesis, Jagiellonian University of Cracow, Poland (2006).
53. T. Liu, PhD Thesis, Paris-Sud XI University, Orsay, France (2010).
54. T. Pérez Cavalcanti, PhD Thesis, Justus Liebig Universität Giessen (2006).
55. A. Rustamov, PhD Thesis, Technische Universität Darmstadt, Germany (2006).
56. S. Spataro, PhD Thesis, Università degli Studi di Catania, Italy (2006).
57. B. Spruck, PhD Thesis, Justus-Liebig-Universität Giessen, Germany (2008).
58. K. Nakamura *et al.*, J. Phys. G **37**, 075021 (2010) *Review of particle physics.*
59. S. Huber, J. Aichelin, Nucl. Phys. A **573**, 587 (1994).
60. A.I. Titov, B. Kämpfer, B.L. Reznik, Eur. Phys. J. A **7**, 543 (2000).
61. M. Betigeri *et al.*, Phys. Rev. C **65**, 064001 (2002).
62. E. Pickup, D.K. Robinson, E.O. Salant, Phys. Rev. Lett. **8**, 329 (1962).
63. J.M. Laget, F. Wellers, J.F. Lecolley, Phys. Lett. B **257**, 254 (1991).
64. T. Vetter, A. Engel, T. Biro, U. Mosel, Phys. Lett. B **263**, 153 (1991).
65. L. Kaptari, B. Kämpfer, Int. J. Mod. Phys. E **19**, 894 (2010).
66. K. Nakayama, Y. Oh, H. Haberzettl, J. Korean Phys. Soc. **59**, 224 (2011).
67. L. Landsberg, Phys. Rep. **128**, 301 (1985).
68. B. Ramstein *et al.*, AIP Conf. Proc. **1257**, 695 (2010).